

Renal Cell Carcinoma subtyping: learning from multi-resolution localization

Mohamad Mohamad^a, Francesco Ponzio^b, Santa Di Cataldo^b, Damien Ambrosetti^c, Xavier Descombes^b

^a*Université Côte d’Azur, INRIA, CNRS, Sophia Antipolis, France*

^b*Politecnico di Torino, Torino, Italy*

^c*Department of Pathology, CHU Nice, Université Côte d’Azur, Nice, France*

Abstract

Renal Cell Carcinoma is typically asymptomatic at the early stages for many patients. This leads to a late diagnosis of the tumor, where the curability likelihood is lower, and makes the mortality rate of Renal Cell Carcinoma high, with respect to its incidence rate. To increase the survival chance, a fast and correct categorization of the tumor subtype is paramount. Nowadays, computerized methods, based on artificial intelligence, represent an interesting opportunity to improve the productivity and the objectivity of the microscopy-based Renal Cell Carcinoma diagnosis. Nonetheless, much of their exploitation is hampered by the paucity of annotated dataset, essential for a proficient training of supervised machine learning technologies. This study sets out to investigate a novel self supervised training strategy for machine learning diagnostic tools, based on the multi-resolution nature of the histological samples. We aim at reducing the need of annotated dataset, without significantly reducing the accuracy of the tool. We demonstrate the classification capability of our tool on a whole slide imaging dataset for Renal Cancer subtyping, and we compare our solution with several state-of-the-art classification counterparts.

Keywords: self supervised learning, digital pathology, renal cell carcinoma subtyping

1. Introduction

Renal Cell Carcinoma (RCC) is a highly malignant tumor and the most widespread type of kidney cancer, accounting for 90% of the overall entities.

Preprint submitted to Computer Methods and Programs in Biomedicine November 15, 2024

This tumor is also the 7th most common histological type in the west, and it is continuously increasing [1]. Its mortality rate is considered high, with respect to its incidence rate, as this tumor is typically asymptomatic at the early stages for many patients [1, 2]. This leads to a late diagnosis of the tumor, where the curability likelihood is lower.

RCC can be categorized into multiple histological subtypes, mainly: Clear Cell Renal Cell Carcinoma (ccRCC) forming 75% of RCCs, Papillary Renal Cell Carcinoma (pRCC) accounting for 10%, and Chromophobe Renal Cell Carcinoma (chRCC) accounting for 5%. Some of the other subtypes include Collecting Duct Renal Cell Carcinoma (cdRCC), Tubulocystic Renal Cell Carcinoma (tRCC), and unclassified [1]. Approximately 10% of renal tumors belong to the benign entities neoplasms, being Oncocytoma (ONCO) the most frequent subtype with an incidence of 3–7% among all RCCs [3, 2]. These subtypes show different cytological signature as well as histological features [2], which ends up in significantly different prognosis.

The correct categorization of the tumor subtype is indeed of major importance, as prognosis and treatment approaches depend on it and on the disease stage. For instance, the overall 5-year survival rate significantly differs among the different histological subtypes, being 55–60% for ccRCC, 80–90% for pRCC and 90% for chRCC. This points out the need for the most accurate subclassification [4, 5].

Existing literature emphasizes also the critical role of the differential diagnosis between chromophobe and oncocytoma, known to be arduous and prone to errors due to overlapping morphological characteristics in a relevant number of cases [2, 6, 3].

Currently, the gold standard to classify RCC subtypes consists in the microscopic visual assessment of Hematoxylin and Eosin (H&E) samples, performed by a pathologist through the microscope. These specimens consist most often of physical slides and, in some centers provided with scanner, of virtual slides: the so-called Whole histological Slide Images (WSIs).

The visual diagnosis of the large WSIs is known to be both effort-requiring and time-consuming, resulting in poor alignment between pathologists in some cases. Ultimately, these aspects have a great impact on diagnosis, prognosis and treatment of RCC neoplasms [7].

Computerized methods represent an interesting opportunity to improve the productivity, as well as the objectivity, of the microscopy-based RCC diagnosis [7]. In this regard, recent evidences suggest that Convolutional Neural Networks (CNNs), a famous class of supervised deep learning algo-

rithms, may be proficiently applied to the classification of RCC subtypes [7]. This is mainly due to the CNNs’ capability to discover unseen data structures and extract robust features representation [7, 8]. Nonetheless, much of their strength depend on the exploitation of large labeled datasets: CNNs are data-hungry supervised algorithms, which demand a large amount of annotated training sample to learn an effective data representation [9, 10]. This aspect is a strong limitation, especially in the histological field [11], where the samples annotation requires a skilled pathologist to visually scrutinise each WSIs and to divide it into sub-regions, homogeneous in terms of tissue architecture, lastly assigned to a corresponding label. This approach, known in the literature as “Region Of Interest (ROI)-cropping procedure” [11], is known to be tedious and time consuming for the pathologist, and also prone to error as well, with the concrete risk of compromising the models training phase due to an inaccurate labelling.

As a consequence, Self-Supervised Learning (SSL) has been recently attracting considerable interest, being able to describe data structures via robust featurization, without requiring any supervision in term of samples annotations [9, 12]. Unfortunately, most self-supervised techniques exploit natural-scene image properties, which are not suitable for histopathology specimen, as evidenced by some recent works [9, 12].

This study sets out to assess RCC subtype classification, based on WSIs, leveraging a novel self-supervised paradigm. Our solution, inspired by the decision-making procedure of the pathologist, incorporates features learnt at different magnification level. With our experiments, we show that through histologic-specific SSL paradigm, it is possible to classify the four most common RCC subtypes with performance comparable to the fully supervised solutions, but without requiring massive data annotation.

2. Background

2.1. RCC subtyping

Much of the studies on RCC subtyping come from the exploitation of the TCGA database [4, 5, 13], without furnishing results at the WSI level [4, 5] or at the patient-level [4, 5, 13]. Furthermore, much of the current literature considers only two [14, 15] (or three [4, 5, 13, 16]) RCC main malignant tumor subtypes: ccRCC and pRCC (and chRCC). This is mainly due to the fact that, being dedicated to malignant tumors, TCGA data portal excludes renal oncocytoma cases.

A considerable part of these studies seek to evaluate the performance of canonical machine learning pipelines, based on morphological or textural hand-crafted features, to discriminate between two [14, 15] or three [16] classes of RCC subtypes. A more recent work by Fenstermak and colleagues, investigated a CNN-based strategy to classify a selection of 3486 patches retrieved from WSIs, and belonging to three classes of interest: ccRCC, pRCC and chRCC. The authors achieved a patch-level accuracy up to 99%, but they do not provide the WSI-level statistics [4].

Although these works are significant in view of the feasibility of an automatic RCC subtyping framework, they suffer from two main limitations: i) they do not take into consideration the difficult differential diagnosis between chRCC and ONCO; ii) they rely on data annotation, requiring the ROI-cropping procedure previously defined.

Answering the first limitation, in 2021, Zhu et al.[17] investigated the RCC subtype classification in more than three classes, including the oncocytoma one. In their study, the authors designed a classification process trained on a proprietary dataset and then tested on TCGA and biopsy database. Nonetheless, the proposed strategy is fully supervised, requiring a massive WSIs annotation to proficiently train the employed ResNet18 classifier. A more recent study by Ponzio et al., proposed a 4 classes RCC subtype categorization through a tree-based classification pipeline [7]. The authors proposed a supervised deep learning solution which leverages pathologist’s expertise and decision-making algorithm to substantially improve the classification performance of state-of-the-art CNN models. Although interesting, the proposed methodology was still based on massive labelled dataset, being built on top of several backbone CNNs classifier.

Up to our knowledge, no published study investigates the RCC subtyping task with SSL paradigm, although previous research has established that histological classification can be proficiently faced with self-supervised methodologies, as detailed in the next subsection.

2.2. Self-supervised learning in histology

Self-supervision was introduced as a solution for annotation-hungry models in their application domains. SSL exploits labels obtained from the data itself, through a semi-automatic process, to delineate a supervised *pretext* task capable of learning an effective representation of the original data. Although the pretext task conducts the learning by means of a supervised loss function, the performance of the model on the pretext is peripheral, being

only a means of getting a general and powerful data representation, capable of solving a number of practical downstream tasks. Most of the popular SSL techniques, among which rotation prediction [18], jigsaw puzzles [19] or image colorization [20], were created and tested primarily for natural images. Therefore, using these raw techniques without any modification, may not produce the desired results in other domains [9]. For instance, in histopathology at the cellular level, objects like cells and nuclei have symmetrical shapes, which are invariant with respect to rotation. Additionally, the tissue region is homogeneous, making it difficult to allocate patches or identify their relative positions using only them as the model’s input. It is simply a problem with no definitive solution.

For this reason, a number of recent studies have proposed SSL strategies specifically suited for histopathology classification. Koohbanani et al. [21] introduced three novel strategies for WSI data, comparing them with standard SSL approaches on different cancer classification datasets. The authors developed a magnification prediction task, where a CNN is fed with patches taken at different magnification levels and learnt to predict their corresponding level. The second task, called jigsaw, is inspired by the jigsaw puzzle [19], where the network should identify the magnification ordering scheme of a sequence of four images. Images are taken out of four different levels, stacked randomly in a square, and fed to the model which assigns them to one of twenty-four possible outputs. Lastly, they modified image colorization to make it more suitable for histopathology, by identifying nuclei through segmentation of hematoxylin channel pixels. Then, the authors compared their three pretext tasks to several canonical SSL strategies, such as rotation and flipping prediction, autoencoder, and generative models, on three cancer classification datasets. They show that the novel histology-specific tasks perform better than the standard ones by a significant margin, especially in low annotation regimes.

Boyd et al. [22] deployed an improved version of a well-known unsupervised learning task, known as visual field expansion, which aims at creating a wider view of an existing image, and employed it as a SSL pretext task. By taking a crop of an initial image, an autoencoder-inspired network can be used to expand the crop and form the entire image. The authors’ model leverages the adversarial autoencoder framework [23], and their objective contains three losses: a reconstruction and two discriminator losses. The first discriminator loss is applied at the latent space level to ensure the contextual representation conforms to a predefined distribution. The second loss is at the generated

image level, where the discriminator tries to distinguish between real and expanded images.

More recently, Srinidhi et al. [24] proposed a three-phase training scheme, termed *Resolution Sequence Prediction* (RSP), that integrates SSL, semi-supervised learning, and consistency learning. Their self-supervised task, is a variation of the magnification puzzle, presented in the work by Koohbanani et al. [21]. The main differences lie in two aspects: first, the inputs are processed as a sequence of three independent images, transforming them into latent vectors, which are then fused to produce a prediction, while jigsaw stacks all four images in a single input. Second, for RSP, they ensure every patch is taken from the center of the lower resolution one. After pretraining the network with RSP, the authors fine-tune it on the main task with the available annotations. In the last phase, they combine consistency learning [25] and teacher-student semi-supervised paradigm to calculate a consistency loss mixed with a supervised cross-entropy loss to train the model.

One significant theme emerges from the studies discussed so far: the importance of low and high magnifications and the various features available at each level. Nonetheless, the role played by the interconnection between the patches taken from the different levels, has not been closely examined.

A recent study by Ding et al. [26] tackled this point by designing a pretext task where the model learns to understand if a magnified patch lies inside or outside of a zoomed-out one. They found that this simple task outperforms magnification predictions and other techniques, including transfer learning, in lung adenocarcinoma subtyping.

Taking inspiration from this latter study, we propose a novel approach based on the concept of inter-level connectivity, which we prove to be more accurate with respect of the above-mentioned SSL solutions in the RCC subtyping task.

3. Materials and methods

3.1. Patients cohorts and dataset

In our database, we collected tissue samples from 91 consecutive patients, who encountered nephrectomy in the Nice Hospital Urology Department, diagnosed with ccRCC (n=56), papRCC (n=22), chrRCC (n=6) or ONCO (n=7). As defined by the 2022 WHO criteria, the diagnosis was based on pathology and cytogenetic analysis. H&E stained WSI (scanned using a Leica AT2 Digital Slide Scanner, Leica Microsystems CMS GmbH, Wetzlar,

Subtypes	Train	Test	Total
ccRCC	33	23	56
pRCC	15	7	22
Onco	3	4	7
Chromo	3	3	6
Total	54	37	91

Table 1: Patients distribution among dataset folds and RCC subtypes

Germany) used for diagnosis were gathered to define a dataset consisting in a total of 201 WSIs. The mean number of slides per subject is $2.2(\pm 1.9)$. From the whole WSIs dataset, with the supervision of two skilled pathologists, ROIs depicting the five classes of interest (namely, healthy renal tissue, ccRCC, papRCC, chrRCC, ONCO) were extracted. Each category is equally represented in the ROIs dataset.

3.2. Formulation

Suppose a WSI has N magnification levels, where 0 is the base level, featuring the lowest resolution, and N is the maximum, providing the highest-resolution images of smaller areas of the tissue (see Figure 1).

We can denote as p_t a generic patch, taken from the WSI at level t , with size (W_t, H_t) . At a higher magnification level $t + 1$, p_t is represented by a higher magnification patch having size $(W_{t+1} = 2 \times W_t, H_{t+1} = 2 \times H_t)$, being the zoom factor between two consecutive levels $\times 2$. Thus, as shown in Figure 1, p_t can be represented as 4 non-overlapping patches in level $t + 1$, each one having the same dimensions as p_t . The formulation of our SSL task specifically relies on such relation between patches in different WSI levels, as detailed in the following.

Consider two resolution levels x and $y \in [0 \dots N]$, such that $y < x$, and let p_y be a patch extracted from level y (see Figure 2(a)). We can term $C_{x|y}$ the set in x containing all the non-overlapping patches that jointly describe p_y .

Lastly, let $p_x \in C_{x|y}$ be a patch belonging to level x , randomly extracted from $C_{x|y}$. The objective in our pre-text task is the prediction of the location of p_x inside p_y .

We formalize our task as a classification problem by randomly sampling a patch from set $C_{x|y}$, which consists of 4^n patches, being $n = y - x$ the

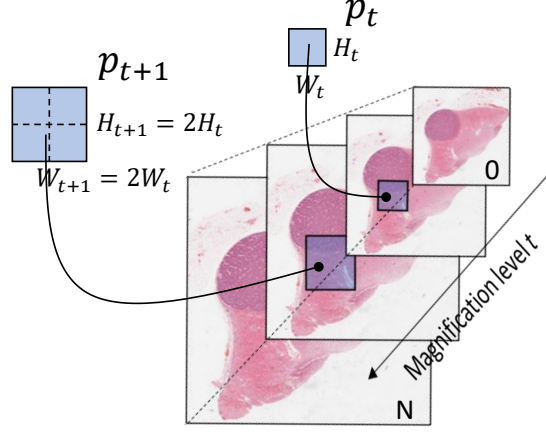


Figure 1: The typical pyramidal structure of a WSI: a collection of images that represents the same content at different magnification levels.

difference between the two magnification levels taken into account. The ground-truth label is generated using the index of p_x in $C_{x|y}$. We use the cross-entropy loss function to measure the discrepancy between the predicted class probabilities and the actual class labels. In the classification formulation, the representation of labels can pose some flexibility. Specifically, the range of the ground-truth is dependent on n , which is equal to $y - x$. To ensure that such range is consistent during the training, as well as during the inference phase, we need to freeze the difference between x and y . In other words, we are free to extract patches from different levels, but the zooming difference between the two levels must remain fixed.

To train our model on the pre-text task, we employed the pipeline shown in Figure 2(b). We applied distinct augmentations to patches p_x and p_y . The former is augmented both geometrically and on the color space, while the latter undergoes only color transformations (further details will follow in the next section). We found that the data augmentation phase helps to lower the over-fitting and to add robustness, avoiding simple solutions, based the tissue edge or on the white space location. Our backbone convolutional encoder, pretrained on ImageNet as later detailed, processes the augmented images using the same weights for both p_x and p_y . Lastly, their latent vector repre-

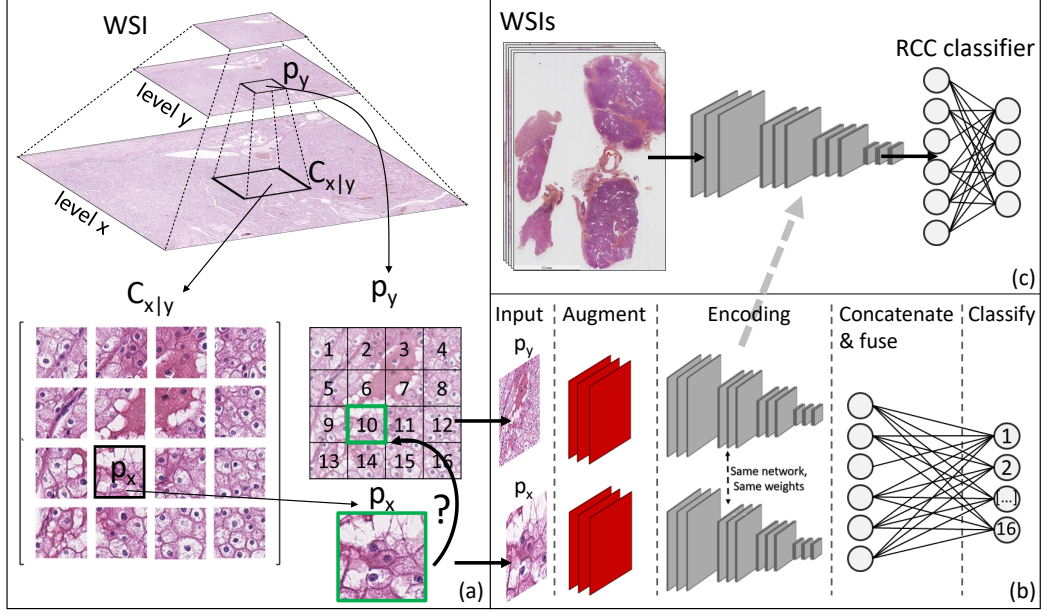


Figure 2: comprehensive picture of the proposed SSL framework including three main panels. (a), the data preparation for our pre-text task. Consider two magnification levels x and y in a given WSI, such that $y < x$. Let p_y be a patch extracted from level y , $C_{x|y}$ the set containing all non-overlapping patches in x and $p_x \in C_{x|y}$. The objective in our pre-text task is to predict the location of p_x inside p_y . (b), the overview of the training pipeline, with the augmentation layers, the shared encoding models for both p_x and p_y , the fusion layer, and the final output classifier, made up of 16 possible classes, namely possible location of p_x in p_y . (c), the knowledge-transfer from the obtained SSL encoding to the main downstream RCC subtyping task.

sentations are fused using a fully connected layer, following the approach of Ding et al. [26]. Once proficiently trained on the pretext task, the backbone’s weights are transferred on the classification level, where are fine-tuned on the RCC subtyping downstream task, as represented in Figure 2(c).

3.3. Implementation details

In this section, we give the implementation details of the proposed architecture.

3.4. The pretext

We split the 91 patients between training and test set, with a split ratio not fixed among the different classes to ensure proper representation of all

the RCC subtypes in the test set (refer to table 1). We start preparing our pre-text task dataset by fixing the zooming difference n between levels x and y equal to two. The patches p_x and p_y , with a size of 256×256 , are extracted randomly such that p_x belongs to one of the three highest magnification levels with probabilities (0.4, 0.4, 0.2). The abundant patches available at higher magnification is the main reason for our choice. To obtain one sample and its label, p_y and its magnified version in level x , namely $C_{x|y}$, are individuated. p_x is randomly sampled from $C_{x|y}$ and its location is one-hot encoded to serve as ground truth for the cross-entropy loss.

Some filtering steps are also implemented to remove images with large white areas. The final dataset, consisting of 784,495 tiles with size 1000×1000 , is further split into training and validation folds (92/8% respectively). As before mentioned, p_y is only augmented with random contrast, while p_x is augmented with random flipping, rotation, contrast, and cropping. The original cropped tiles are re-scaled to 112×112 before augmentation, to minimize computational time. Following the findings in [7], we deploy a VGG16 network as the encoder backbone, changing only the final max pooling layer to an average pooling one. As previously mentioned, both the encoder of p_x and p_y are trained jointly. The two latent vectors are then concatenated in a 1024 vector, fed to a fully connected layer of 256 neurons, and finally to the last layer, made up of 16 outputs (namely, 16 classes or possible locations of p_y in p_x). Training on our pretext task required a very low learning rate of 2×10^{-5} , a batch of 32, and a weight decay of 10^{-5} . We opted for an Adam optimizer. In our experiment, training reached a saddle point early on (this can be due to the small learning rate we had to start with), and defining a scheduler was non-trivial. Specifically, we changed the learning rate twice during training. After the first stall, we increased the learning rate to 10^{-4} . It must be mentioned that implementing cosine warm-up could enhance this approach, but further study is needed to determine the optimal rate of the learning rate increase. At the second stall, we increased the batch size to 64, obtaining a similar effect as decreasing the learning rate, but without suffering its long-run issues.

3.5. RCC subtype classification

We start by dividing the ROIs into 1024×1024 patches at the maximal resolution, filtering out the white background and resizing the rest to 112×112 pixels. We balance and split the resulting data into a training (85%) and a validation subset (15%). For the test set, we follow the same pipeline, except

that we extract patches from the entirety of the WSIs, thus without ROIs. To infer the final patient-wise label, we feed all the patches belonging to a single patient to the network and aggregate the results by a majority voting scheme. The training of the networks, pre-trained using the self-supervised tasks, undergoes two stages. The first is an initialization for the classifier weights where we freeze the backbones and train the network for 4 epochs, the first 2 with a learning rate of 10^{-3} , and the last 2 with a learning rate of 10^{-4} . In the second stage, we unfreeze the backbones and deploy a cosine warmup, which allows the learning rate to reach the maximum value of 10^{-4} within 5% of the total training iterations. We train the models for 120 epochs using a batch size of 2.

3.6. Counterpart models

In our study, we compare the proposed architecture with three counterpart solutions, representing a picture of the different state-of-the-art training paradigms for machine learning models adopted in the classification of histological WSI:

- i) the SSL methodology, proposed by Ding et al [26];
- ii) a canonical CNN pre-trained on the ImageNet dataset and fine-tuned on the RCC classification task
- iii) a fully supervised solution, proved to be the top performing one in this classification scenario in a recent study [7].

3.6.1. SSL methodology

As previously mentioned, the solution by Ding et al. [26] consists of a model which learns a powerful data representation by understanding if a magnified patch lies inside or outside of a zoomed-out one. To put into effect such method, we started from our SSL task dataset and we generated the data by taking a tuple of samples and switching their high-resolution patch with a probability of 0.5. If the patches were switched, both samples became negative samples, and if they were not switched, the samples were considered positive. We used the same fusion scheme and hyper-parameters they used in their experiment and trained until the performance plateau at around 50 epochs.

3.6.2. Imagenet-based

To define a solid transfer learning based counterpart, we refer to our previous work, where we individuated the VGG16 CNN pre-trained on ImageNet

as optimal transfer learning framework in this classification scenario [7]. The model is trained with a batch size of 32 and a learning rate of 10^{-4} for a total of 120 epochs.

3.6.3. Fully supervised solution: the ExpertDT

As fully supervised counterpart, we select *ExpertDT*, a classification model which leverages a combination of supervised deep learning models (specifically CNNs) and pathologist’s expertise to substantially improve the accuracy in the RCC subtyping task [7].

All the counterparts frameworks are trained using Adam optimizer and a weight decay of 10^{-5} . The best-performing models in terms of validation accuracy is always selected and all of them use a linear classifier for the downstream task.

4. Results

A competent SSL framework should ideally have two main characteristics. First, it should be accurate in a way that is not too far from fully supervised solutions. On the other hand, it should be robust and capable of scaling well with the reduction of available dataset, used in the downstream supervised learning task. Thus, we designed two peculiar experiments to test them. Figure 3 shows the outcome of the first set of experiments, reporting the confusion matrices obtained on the RCC subtyping task of our solution (top-left), Ding et al.’s counterpart [26] (top-right), ImageNet-based (bottom-left), and the fully supervised solution ExpertDT [7] (bottom-right). Such confusion matrices report the absolute number of patients correctly categorized (see the main diagonal) and incorrectly assigned (other positions of the grid) for each of the four classes of interest. We were the second-best solution in terms of mean accuracy between classes, following only the supervised one (76.5% ours versus 87% ExpertDT). Furthermore, we outperformed the counterpart SSL methodology by around 12% (76.5% ours versus 64.3% Ding et al.), as well as the ImageNet-based one by more than 6% of mean accuracy (76.5% ours versus 69.8% ImageNet).

In absolute terms, our solution misclassified 11 patients, the SSL counterpart 13, the Imagenet-based 13 as well, while ExpertDT only 10 (all rounded up). By running this set of experiments five times, we were able to also assess the robustness of the solutions tested among different execution of the learning. This aspect is embodied in the standard deviation of the number

Ours					Ding et al. [26]				
ccRCC	20.2 ± 0.8	2.8 ± 0.8	0.0 ± 0.0	0.0 ± 0.0	ccRCC	17.0 ± 1.0	6.0 ± 1.0	0.0 ± 0.0	0.0 ± 0.0
pRCC	0.0 ± 0.0	7.0 ± 0.0	0.0 ± 0.0	0.0 ± 0.0	pRCC	0.0 ± 0.0	7.0 ± 0.0	0.0 ± 0.0	0.0 ± 0.0
chRCC	0.6 ± 0.5	0.2 ± 0.4	1.6 ± 0.5	0.6 ± 0.5	chRCC	1.0 ± 0.0	0.0 ± 0.0	1.0 ± 0.0	1.0 ± 0.0
ONCO	0.2 ± 0.4	0.8 ± 0.4	0.4 ± 0.5	2.6 ± 0.5	ONCO	0.2 ± 0.4	0.8 ± 0.4	1.0 ± 0.0	2.0 ± 0.0
	ccRCC	pRCC	chRCC	ONCO		ccRCC	pRCC	chRCC	ONCO

ImageNet-based					ExpertDT [7]				
ccRCC	17.0 ± 1.7	5.8 ± 1.3	0.0 ± 0.0	0.2 ± 0.4	ccRCC	18.6 ± 1.1	1.4 ± 1.1	1.8 ± 0.4	1.2 ± 0.4
pRCC	0.0 ± 0.0	7.0 ± 0.0	0.0 ± 0.0	0.0 ± 0.0	pRCC	0.2 ± 0.4	6.8 ± 0.4	0.0 ± 0.0	0.0 ± 0.0
chRCC	0.6 ± 0.5	0.0 ± 0.0	1.2 ± 0.8	1.2 ± 0.4	chRCC	0.0 ± 0.0	0.2 ± 0.4	2.4 ± 0.9	0.4 ± 0.9
ONCO	0.0 ± 0.0	0.8 ± 0.4	0.6 ± 0.5	2.6 ± 0.5	ONCO	0.2 ± 0.4	0.0 ± 0.0	0.2 ± 0.4	3.6 ± 0.5
	ccRCC	pRCC	chRCC	ONCO		ccRCC	pRCC	chRCC	ONCO

Figure 3: Confusion matrices obtained on the RCC subtyping task of our solution (top-left), Ding et al.’s counterpart [26] (top-right), ImageNet-based (bottom-left) and the fully supervised solution ExpertDT [7] (bottom-right).

of patients assigned to each class, as reported in Figure 3. We can notice that the proposed solution shows a reasonable low standard deviation coupled with correctly classified patients (see the main diagonal of the top-left confusion matrix of Figure 3).

With the second set of experiments, we assessed the resilience of the different evaluated approaches to the reduction of the size of the learning dataset, employed for the downstream task. Figure 4 shows the mean accuracy of the RCC classification task of the tested approaches, with a progressively reduced size of the learning dataset. We can observe that our solution (see the blue line) is the most performing with only 33% of the available annotated dataset employed for the training, and progressively improves its mean

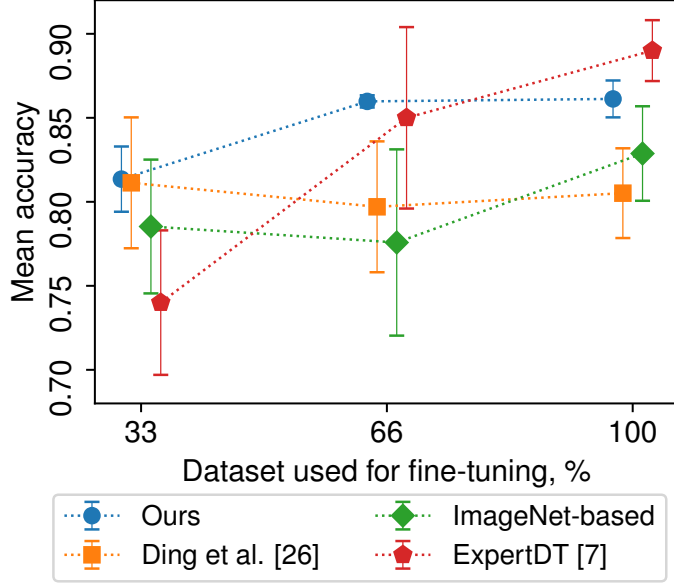


Figure 4: Mean accuracy with standard deviation among five runs (see the error bars) of the RCC classification task of the tested approaches, with a progressively reduced size of the learning dataset. We can observe that our solution (see the blue line) is the most performing with only 33% of the available dataset employed for the training, and progressively improves its mean accuracy with the growing of the training set size. Interestingly, we can not observe a similar behaviour for the other two SSL counterparts (see the green and the orange lines), which both show a reduced accuracy going from 33 to 66 % of the training set size. Lastly, as expected, the fully supervised ExperDT [7] (see the red line), despite being the most accurate with the whole dataset employed for training, it substantially suffers the reduction of the number of the training samples, rapidly decreasing with the reduction of the annotated cohort.

accuracy with the growing of the training set size. Interestingly, we can not observe similar behaviours for the other two SSL counterparts (see the green and the orange lines), which both show a reduced accuracy going from 33 to 66 % of the training set size. Furthermore, the proposed solution presents the lowest standard deviation among the five different runs, as represented by the error bars in Figure 4, which suggests a superior learning robustness with respect to the other considered counterparts. Lastly, as expected, the fully supervised ExperDT [7] (see the red line), despite being the most accurate with the whole dataset employed for training, it substantially suffers the reduction of the number of the training samples, rapidly decreasing in mean accuracy with the reduction of the annotated cohort.

5. Discussion

In this study, we proposed a frontier SSL approach based on the concept of inter-level connectivity of WSI, which mimics the reasoning and the procedure of a pathologist, diagnosing RCC lesions. The comparison between our solution and different baselines reveled a number of interesting aspects.

First, despite being substantially less accurate with respect to a fully supervised solution, our method outperforms the recent SSL procedure proposed by Ding et al [26], as well as a common baseline made up of an ImageNet-pretrained CNN, fine tuned on the final classification task.

Our solution seems also to be quite robust among different runs of the learning procedure, showing relatively low variations of the classes assigned to the different collected subjects. This can be evinced from both the standard deviations reported in Figure 3, and the error bars of Figure 4.

Additionally, the proposed methodology shows a good robustness in presence of a progressively reduced size of the annotated training set. This aspect is paramount, as it is the main reason of researching learning solutions able to minimize the needing of annotations, which are costly, especially in the pathology domain. Our method still performs with a mean accuracy above 80% with only 33% of employed training set. This suggests superior robustness with respect to the two SSL counterparts, although, as expected, both of them mitigate the performance degradation, caused by the reduction of the employed training set, especially when compared to the supervised methodology. Indeed, with only 33% of the training set employed for the learning, the supervised solution classifies with a mean accuracy below 75%, which is more than 8% lower than our SSL methodology. This largely assess the goodness of the proposed pre-text task, which significantly reduces the amount of required annotated samples, with respect to a canonical supervised learning.

As future directions, we intend to expand our dataset with other RCC cancers, including rare subtypes and classes. Moreover, we intend to investigate the performance of the proposed solutions in other histological domain, to assess the portability of the system in other cancer subtyping tasks.

References

- [1] J. Hsieh, M. Purdue, S. Signoretti, C. Swanton, L. Albiges, M. Schmidinger, D. Heng, J. Larkin, V. Ficarra, Renal cell carcinoma, *Nature Reviews Disease Primers* 3 (2017) 17009. doi:10.1038/nrdp.2017.9.

- [2] L. D. Truong, S. S. Shen, Immunohistochemical diagnosis of renal neoplasms, *Archives of pathology & laboratory medicine* 135 (1) (2011) 92–109.
- [3] S. K. Tickoo, M. B. Amin, Discriminant nuclear features of renal oncocytoma and chromophobe renal cell carcinoma: analysis of their potential utility in the differential diagnosis, *American journal of clinical pathology* 110 (6) (1998) 782–787.
- [4] M. Fenstermaker, S. A. Tomlins, K. Singh, J. Wiens, T. M. Morgan, Development and validation of a deep-learning model to assist with renal cell carcinoma histopathologic interpretation, *Urology* 144 (2020) 152–157.
- [5] S. Tabibu, P. Vinod, C. Jawahar, Pan-renal cell carcinoma classification and survival prediction from histopathology images using deep learning, *Scientific reports* 9 (1) (2019) 1–9.
- [6] A. B. Rosenkrantz, N. Hindman, E. F. Fitzgerald, B. E. Niver, J. Melamed, J. S. Babb, Mri features of renal oncocytoma and chromophobe renal cell carcinoma, *American Journal of Roentgenology* 195 (6) (2010) W421–W427.
- [7] F. Ponzio, X. Descombes, D. Ambrosetti, Improving cnns classification with pathologist-based expertise: the renal cell carcinoma case study, *Scientific Reports* (2023).
- [8] F. Ponzio, G. Urgese, E. Ficarra, S. Di Cataldo, Dealing with lack of training data for convolutional neural networks: The case of digital pathology, *Electronics* 8 (3) (2019) 256.
- [9] A. Mascolini, D. Cardamone, F. Ponzio, S. Di Cataldo, E. Ficarra, Exploiting generative self-supervised learning for the assessment of biological images with lack of annotations, *BMC bioinformatics* 23 (1) (2022) 1–17.
- [10] S.-C. Huang, A. Pareek, M. Jensen, M. P. Lungren, S. Yeung, A. S. Chaudhari, Self-supervised learning for medical image classification: a systematic review and implementation guidelines, *NPJ Digital Medicine* 6 (1) (2023) 74.

- [11] F. Ponzio, E. Macii, E. Ficarra, S. Di Cataldo, W2wnet: a two-module probabilistic convolutional neural network with embedded data cleansing functionality, *Expert Systems with Applications* 214 (2023) 119121.
- [12] O. Ciga, T. Xu, A. L. Martel, Self supervised contrastive learning for digital histopathology, *Machine Learning with Applications* 7 (2022) 100198.
- [13] Z. Gao, P. Puttapirat, J. Shi, C. Li, Renal cell carcinoma detection and subtyping with minimal point-based annotation in whole-slide images, in: *International Conference on Medical Image Computing and Computer-Assisted Intervention*, Springer, 2020, pp. 439–448.
- [14] J. Cheng, Z. Han, R. Mehra, W. Shao, M. Cheng, Q. Feng, D. Ni, K. Huang, L. Cheng, J. Zhang, Computational analysis of pathological images enables a better diagnosis of tfe3 xp11. 2 translocation renal cell carcinoma, *Nature communications* 11 (1) (2020) 1–9.
- [15] R. Xiao, E. Debreuve, D. Ambrosetti, X. Descombes, Renal cell carcinoma classification from vascular morphology, in: M. de Bruijne, P. C. Cattin, S. Cotin, N. Padoy, S. Speidel, Y. Zheng, C. Essert (Eds.), *Medical Image Computing and Computer Assisted Intervention – MICCAI 2021*, Springer International Publishing, Cham, 2021, pp. 611–621.
- [16] S. Chen, N. Zhang, L. Jiang, F. Gao, J. Shao, T. Wang, E. Zhang, H. Yu, X. Wang, J. Zheng, Clinical use of a machine learning histopathological image signature in diagnosis and survival prediction of clear cell renal cell carcinoma, *International Journal of Cancer* 148 (3) (2021) 780–790.
- [17] M. Zhu, B. Ren, R. Richards, M. Suriawinata, N. Tomita, S. Hassanpour, Development and evaluation of a deep neural network for histologic classification of renal cell carcinoma on biopsy and surgical resection slides, *Scientific reports* 11 (1) (2021) 1–9.
- [18] S. Gidaris, P. Singh, N. Komodakis, Unsupervised representation learning by predicting image rotations (2018). doi:10.48550/ARXIV.1803.07728.
URL <https://arxiv.org/abs/1803.07728>

- [19] M. Noroozi, P. Favaro, Unsupervised learning of visual representations by solving jigsaw puzzles (2016). doi:10.48550/ARXIV.1603.09246.
URL <https://arxiv.org/abs/1603.09246>
- [20] R. Zhang, P. Isola, A. A. Efros, Colorful image colorization (2016). doi:10.48550/ARXIV.1603.08511.
URL <https://arxiv.org/abs/1603.08511>
- [21] N. A. Koohbanani, B. Unnikrishnan, S. A. Khurram, P. Krishnaswamy, N. Rajpoot, Self-path: Self-supervision for classification of pathology images with limited annotations (2020). doi:10.48550/ARXIV.2008.05571.
URL <https://arxiv.org/abs/2008.05571>
- [22] J. Boyd, M. Liashuha, E. Deutsch, N. Paragios, S. Christodoulidis, M. Vakalopoulou, Self-supervised representation learning using visual field expansion on digital pathology (2021). doi:10.48550/ARXIV.2109.03299.
URL <https://arxiv.org/abs/2109.03299>
- [23] A. Makhzani, J. Shlens, N. Jaitly, I. Goodfellow, B. Frey, Adversarial autoencoders (2015). doi:10.48550/ARXIV.1511.05644.
URL <https://arxiv.org/abs/1511.05644>
- [24] C. L. Srinidhi, S. W. Kim, F.-D. Chen, A. L. Martel, Self-supervised driven consistency training for annotation efficient histopathology image analysis, Medical Image Analysis 75 (2022) 102256. doi:10.1016/j.media.2021.102256.
URL <https://doi.org/10.1016%2Fj.media.2021.102256>
- [25] Q. Xie, Z. Dai, E. Hovy, M.-T. Luong, Q. V. Le, Unsupervised data augmentation for consistency training (2019). doi:10.48550/ARXIV.1904.12848.
URL <https://arxiv.org/abs/1904.12848>
- [26] R. Ding, A. Yadav, E. Rodriguez, A. C. A. L. da Silva, W. Hsu, Improving the self-supervised pretext task for histopathologic subtype classification, in: Medical Imaging with Deep Learning, 2022.
URL <https://openreview.net/forum?id=7QWzEwByMXq>